Editors' Suggestion

Characteristic rupture height of the mediating air film beneath an impacting drop on atomically smooth mica

Ramin Kaviani and John M. Kolinski*
EMSI Laboratory, École Polytechnique Fédérale de Lausanne, 1015 Lausanne, Switzerland

(Received 24 February 2023; accepted 22 September 2023; published 31 October 2023)

Before a droplet can contact a surface during impact, it must first displace the air beneath it. Over a wide range of impact velocities, the droplet first squeezes the air into a thin film, enhancing its resistance to drainage; this slows the progress of the liquid toward the surface. Indeed, below a critical impact velocity, the air film remains intact, and the droplet rebounds off of the air film without making contact. For impact velocities exceeding this critical impact velocity, the droplet always makes contact. The initiation of contact formation requires a topological transition, whereby the initially connected gas domain is ruptured and a liquid capillary bridge forms, binding the droplet to the surface. Here we probe this transition in detail around the critical impact velocity using calibrated total internal reflection microscopy to monitor the air film thickness and profile at high speed during the impact process. Two air film rupture modalities are observed: nucleated contacts, which are isolated and do not correspond to the global minimum air film thickness, and spontaneous contacts, which occur always on a ring centered upon the impact axis where the air film reaches its global minimum. Our measurements show that for impact velocities exceeding the critical velocity for contact initiation, the air film ruptures at a nearly identical height $h_{\min} \approx 20$ nm, for two fluids: silicone oil and a water-glycerol mixture. The height and time duration of the air film prior to contact are presented for over 180 droplet impact experiments. Impact events of water solution droplets show statistics for contact nucleation different from those for the silicone oil; this suggests that another mechanism may dominate contact nucleation during impact of the solution. Nevertheless, a critical impact velocity above which contact always occurs is identifiable for both liquids.

DOI: 10.1103/PhysRevFluids.8.103602

I. INTRODUCTION

The initial formation of contact between a liquid and a solid surface is typically mediated by a third medium, most often in our daily experience, air. Indeed, when a droplet of water impacts a solid, it makes contact imperceptibly quickly, a transition so rapid that it occurs much faster than we can observe with the unaided eye. However, from a continuum perspective, we know the gas must be punctured, or otherwise disrupted, for liquid-solid contact to form. The process of droplet impact is at the center not only of our daily experience, but also in myriad industrial settings such as heat transfer, fuel injection, and inkjet printing [1]. The role of air in droplet impacts has been thoroughly studied, from its initial formation and evolution [2–9] to the noncontact bouncing transition [10–12] to postcontact wetting [13–16]. Vapor emanating from the impacting droplet, either during impact on heated surfaces [17,18] or by effervescence [19], can also prevent contact with the solid surface. It is clear that over a wide range of impact velocities, despite the ubiquity and applicability of droplet

*john.kolinski@epfl.ch

impact mechanics, the key phase of air film disruption and the formation of contact remain to be precisely quantified.

Although the air film formation and rupture phenomenon have been identified in prior work and it is clear that the air film thickness evolves relatively slowly [8], there are striking discrepancies in the value of the air film thickness immediately prior to contact that are reported by different experimental studies [3,14,20,21] ranging from 1–2 nm to several hundred nanometers. With this large spread in the measured air film thickness prior to rupture, the mechanism responsible for the instability of the air film has not yet been conclusively determined. Indeed, various mechanisms ranging from spinodal dewetting [3,22–24] to gas kinetic effects [6,12,25] to electrostatics [26] or surface roughness [27,28] have been identified as possible causes for air film rupture; however, the spread in the data of the measured air film thickness prior to rupture makes it impossible to distinguish between the various mechanisms that may dominate these dynamics. Thus, a fundamental and important question of what drives liquids into contact with solid surfaces through an intervening gas remains open, with implications for coating flows [29] and splashing [30].

In this paper we present measurements of the temporal evolution of the air film that are calibrated to $+7$ or -3 nm. To achieve this calibration, we employ two optical methods that are used simultaneously to ensure rigorous calibration of the measurement: total internal reflection microscopy (TIR) [3,31] and single-color interferometry (FIF) [32]. Once the simultaneous imaging yields a calibrated TIR measurement with a prescribed displacement of a precision piezoelectric stage, we use the higher-precision TIR measurement to image the liquid-air interface during droplet impact over a velocity range from 0.3 to 0.9 m/s on freshly cleaved, atomically smooth mica substrates at high speeds [80000 frames/s (fps), Photron Nova S12]. This velocity range contains the rebound-to-wetting transition [10] for both water-glycerol and silicone oil droplets. To control the impact velocity precisely, droplets are released from a luer tip, with a diameter selected to yield identically sized droplets of either water and glycerol or silicone oil. To establish good statistics of the impact dynamics, multiple impacts were carried out at each impact velocity. Analysis of the recorded film profiles yields the height of closest approach prior to rebound, h^*, obtained by azimuthally averaging the data for a single event, or the height of closest approach, obtained at each pixel where air film rupture is observed $h_{\min}$.

Despite the great care we take in preparing the mica surfaces, nucleation of contact is nevertheless occasionally observed, more often for the water-glycerol solution than for the silicone oil; the time to wait between air film formation and eventual rupture, t_c, is recorded for each event. The $t_c(h_{\min})$ data are then plotted. We comment on how this observation might prove useful in future numerical calculations and its importance to liquid-solid contact formation more generally.

II. EXPERIMENTAL SETUP AND METHODS

The experimental setup consists of two distinct optical paths corresponding to the TIR and FIF experimental methods used to characterize the liquid-air interface beneath the impacting drops. The first path, dedicated to the TIR measurement, directs coherent laser light to strike the impact surface obliquely from below, whereas the second path, dedicated to the FIF measurement, directs light from a weakly coherent ($\ell_{\text{coh}} \approx 2.5$ μm) such that it is normally incident upon the impact surface from below; the key components for each optical path are depicted schematically in Fig. 1(a). Such simultaneous profilometry provides complementary data for interfacial mechanics [24,33–35]. The liquid-air interface prior to contact initiation is depicted schematically in Fig. 1(b). To control the impact velocity U, we vary the height H from which the droplet is allowed to fall; due to the residual oscillations of the droplet prior to impact, a weak nonlinearity of U emerges as a function of H, as shown in Fig. 1(c). Two example time-synchronized image series, recorded with the two respective optical paths, are depicted in Figs. 1(d) and 1(e).

To probe the stability of the air film, the defects commonly encountered on even carefully cleaned glass surfaces must be avoided. This requires a solid surface that will be devoid of material defects over an area of at least approximately 1 mm^2. To obtain such "perfect" surfaces, we cleave sheets

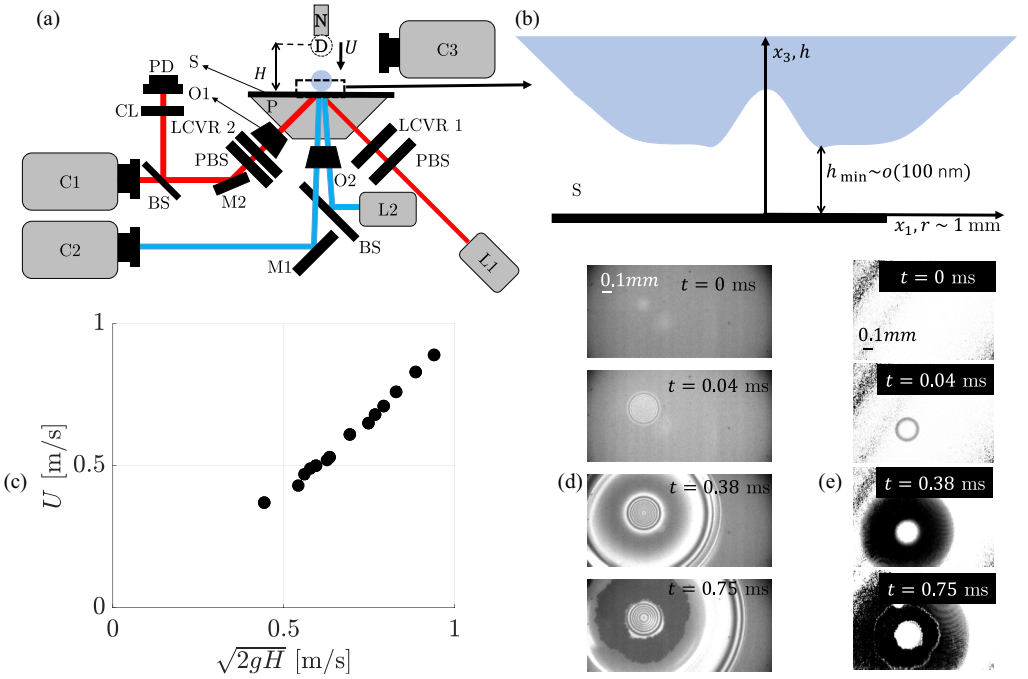

FIG. 1. (a) Schematic layout of simultaneous TIR and FIF microscopy for the study of droplet impact. The setup is calibrated to have an accuracy of $+7$ or -3 nm for air layer thickness measurements below 300 nm in the x_3 direction (see Appendix A for details on the calibration procedure). The liquid drops with diameter $D \approx 2$ mm fall from the height H from the nozzle (N) on a mica substrate (S), reaching a maximum velocity of U. We cleave a mica slab through its thickness to obtain an atomically flat surface over several millimeters in the x_1-x_2 plane. We optically couple the mica sheets to the dove prism (P) made from BK-7 glass by immersion oil. In the TIR microscopy optical path, coherent light emitted by the laser source (L1) illuminates S at incident angles greater than the critical angle for the solid-air interface. We use the polarizing beam splitters (PBS) and liquid-crystal variable retarders (LCVR) to ensure that the light arrives at the substrate-air interface linearly p polarized. The light is totally internally reflected from the mica-air interface beneath the impacting droplet. Half of the reflected light is captured by camera C1 and the second half is concentrated on a photodiode sensor (PD) by a condenser lens (CL). The PD is required for measuring the optical properties of substrate S, as explained in Appendix A. The FIF data are acquired using a second optical path. Light emitted from a high power LED light source (L2) passes through the beam splitter (BS), reflects from the impact interface, and is captured on camera C2. Two dry 5× Mitutoyo microscope objectives O1 and O2 are used for magnification. The monochromatic fast cameras C1 and C2 are fitted with tube lenses (not shown) and are synchronized to record images at 80 000 fps. Mirrors M1 and M2 are used to align the light. We use a third camera C3 recording at 8000 fps to measure U. (b) Region underneath the droplet just before contact initiation shown schematically with an exaggerated x_3 axis. The air forms a nanometer-scale lubrication layer, at the periphery of a dimple centered upon the impact axis. (c) Impact velocities U ranging from 0.34 to 0.91 m/s, are controlled by changing H. Example image series of the air film formation and rupture are captured with the (d) FIF and (e) TIR imaging modalities, shown at three time steps. After postprocessing, the light intensities can be converted to the air film thicknesses for each image; the temporal evolution is recovered by evaluating the time series of images. The dimple region centered upon the impact axis of the droplet is clearly visible; it extends a few microns from the impact surface, as can be seen from the fringe rings in the FIF images. This region resides outside the penetration depth of the TIR imaging modality and is identifiable from the bright circles centered upon the impact axis in the TIR images.

of high-grade mica through their thickness, generating an atomically smooth surface over several mm^2. Experiments are conducted with two different liquids: water-glycerol solution droplets with $D = 1.91$ mm and silicone oil with $D = 1.83$ mm. We used silicone oil with a viscosity of 10 cSt and prepared the water-glycerol solution mixture to have the same kinematic viscosity. The densities of the solution and oil are 1168.1 kg/m^3 and 937.1 kg/m^3, respectively. The surface tension for the solution (68.0 mPam) is greater than of the oil (20.2 mPam) as measured by pendant drop method. Both liquids wet the mica surfaces with contact angles below the resolution of our side-on microscopy imaging modality. The finite viscosity of the liquid is used to suppress high-frequency oscillations that can rupture the air film upon the center of the impact axis [36] and suppress droplet rebound.

Mica is a weakly birefringent solid and can alter the polarization of the light used in the TIR optical path. The birefringence of the mica can be pre- and postcompensated with liquid-crystal variable retarder plates, ensuring strict control over the state of polarization at the reflecting surface, where the droplet will impact the surface. While prior studies suggest an analytical means of calibrating the transfer function from intensity to height [15,31], we used complementary optical methods to perform a direct calibration using a precision piezoelectric stage, as described in detail in Appendix A. The concurrent imaging with TIR and FIF provides complimentary information about the liquid-air-solid interface: TIR can resolve air layer thicknesses up to approximately 500 nm, whereas FIF can visualize the air film profile of up to several microns [37]. In FIF, the film profile is encoded in a two-dimensional fringe pattern, where the intensity of the fringes indicates the optical interference at a given spatial location within the image. While the FIF fringe patterns can be demodulated to provide absolute film measurements that are up to few microns thick, we only analyze the regions where the film thickness is less than half of the light wavelength, or approximately 200 nm.

Our microscopy setup has a resolution of 3.6 μm in the x_1-x_2 plane. In the x_3 direction, the resolution of profilometry is as low as +7 or − 3 nm, but the calibrated field of view has a ceiling at about 350 nm. The threshold of unstable air gap thicknesses (h^* and h_{min}) falls within the calibrated range of our imaging modalities. As the dynamics of droplet rebound and air film rupture are very rapid, high-speed imaging is employed to attain relevant temporal information from our experiments. Light from the two optical paths is imaged onto the sensors of synchronized high-speed cameras (Photron Nova S12) and the sensor data are recorded at 80 000 fps. The sequence of images in Figs. 1(d) and 1(e) shows the rapid nature of air film formation, its rupture, and surface wetting.

III. AIR FILM FORMATION AND RUPTURE

At the early stage of a low-speed impact, the liquid skates over the air [3], increasing the lateral extent of the air film. In this regime, the droplet entrains the air at the leading edge of the drop and depending on the liquid viscosity can lift away from the surface [8], generating the extended liquid-gas interface above the solid. The extended air film drains very slowly and remains stable provided it does not approach within a critical distance of the surface [10]. Indeed, for sufficiently slow impacts, the droplet will reliably rebound from the air film [10], as shown in Figs. 2(a)–2(c). This indicates a threshold height of closest approach h^* that decreases as the impact speed increases [Figs. 2(d) and 2(e)]. The bouncing to wetting transition velocity for the oil droplets (0.6 m/s) is higher than that of the solution (0.53 m/s). At the same time, the silicone oil droplet reliably approaches closer to the surface: $h^* = 32$ (+7 or − 3) nm for the oil, while $h^* = 60$ (+7 or − 3) nm for the solution. The height traces for several U, recorded at the radius where h^* is observed, are shown for the solution droplet in Fig. 2(f).

The initial formation of contact, via a topological transition from a coherent air film to a locally ruptured air film, is observed to occur in two distinct manifestations. First, and most commonly, the air film ruptures locally, at an isolated contact, independently of the relative location of the globally minimal air film thickness. Such events clearly nucleate at a surface imperfection, owing to the proximity of the liquid to the solid over the extent of the thin air film. The outward-advancing

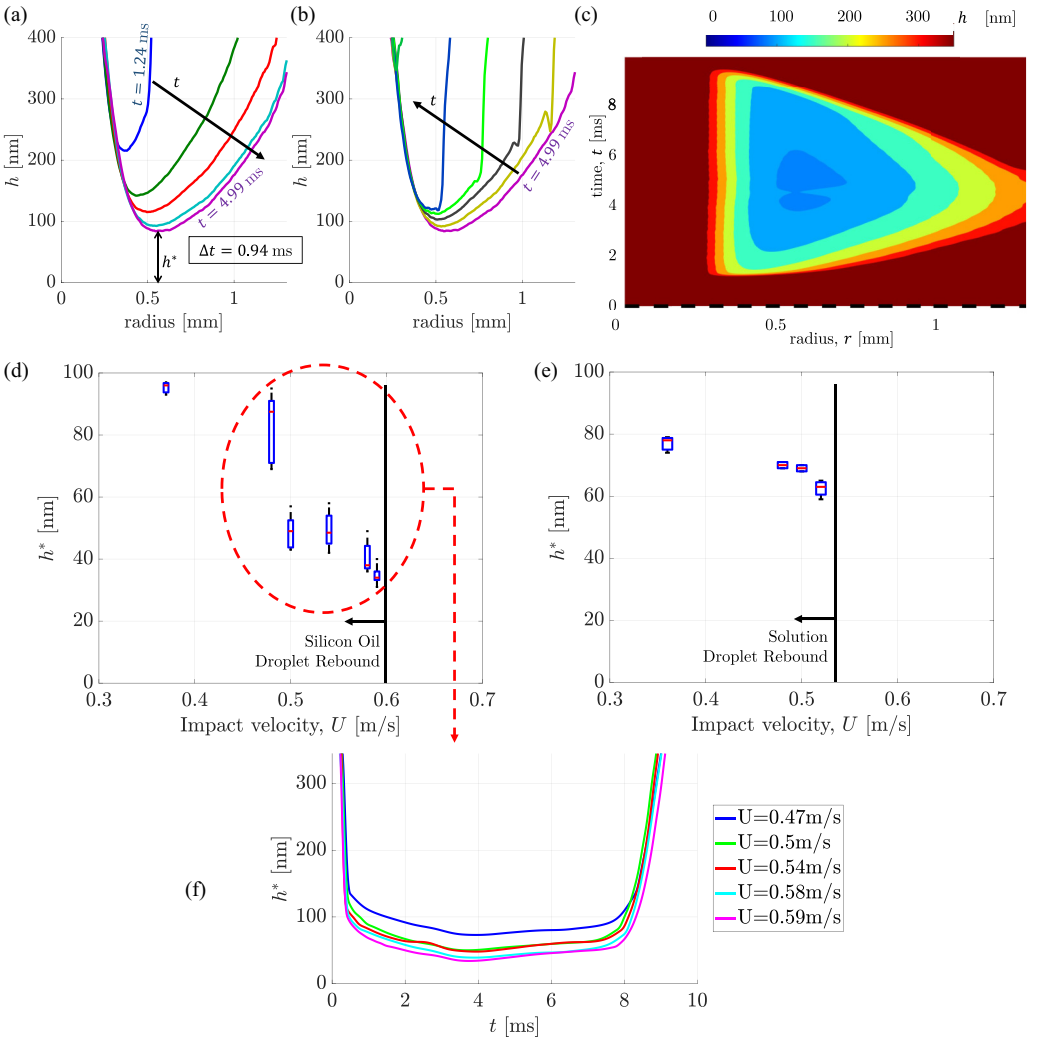

FIG. 2. Below a critical impact speed, the air film under the droplet is stable and causes the droplet to rebound from the mica substrate. As an example for $U = 0.5$ m/s, the 10-cSt water-glycerol droplet pushes the air layer, creating a time-dependent profile h which is drawn based on the radius r from the center of the impact in (a) and (b) for a few time steps. The data are truncated at the maximum gap thickness of 350 nm, which is the limit of the calibrated range of our microscopy setup. Time t is measured from the moment the droplet enters the FIF field of view $h(0, t = 0) = O(10^{-6})$ m. (c) Data from (b) plotted with h in color according to the color bar for continuous t. For impact velocities beyond a threshold, the air layer is always unstable and wetting is initiated. This indicates a limiting stable film height h^*; this height of closest approach decreases gradually with higher velocities, as shown for (d) silicone oil and (e) water-glycerol solutions. Open blue boxes indicate the range from the bottom to the top quartile, red lines indicate median values, and black whiskers indicate absolute maximum and minimum values. The critical rebound velocity for the oil droplets (0.6 m/s) is higher than that of the solution (0.53 m/s). (f) The $h(t)$ variation close to critical impact velocity is presented for the solution. The minimum captured h^* for the oil, at 32 nm, is lower than the solution, at 59 nm.

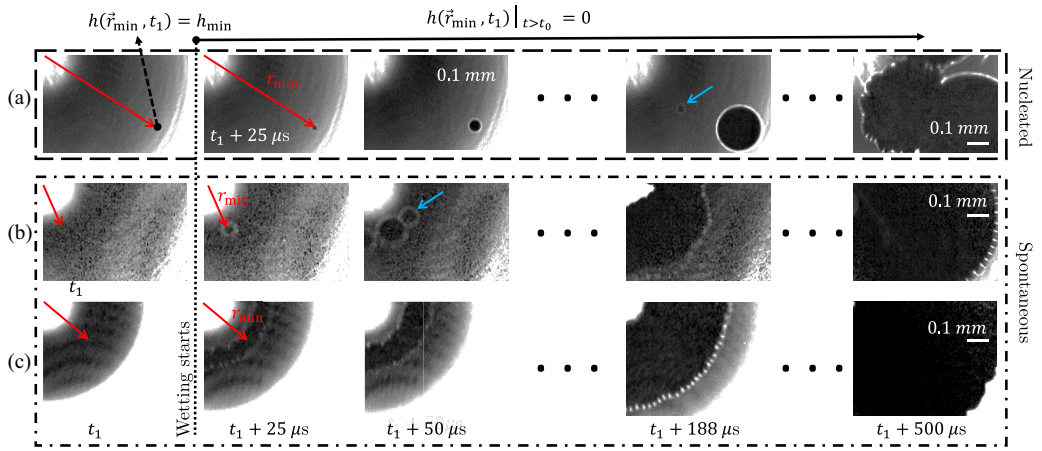

FIG. 3. Normalized image series of contact formation from the TIR microscopy for (a) $U = 0.5$ m/s, (b) $U = 0.58$ m/s, and (c) $U = 0.91$ m/s. Surface wetting starts by breaking through a thin layer of air between a mica surface and the liquid. The $h_{\min}$ is recorded locally at $r_{\min}$ (red arrows) at the last frame recorded ($t = t_1$) just before the air film rupture is captured by the high-speed camera. In (a) two nucleated contacts form separately and the contact lines moves radially outward from the respective points of contact formation until they meet. Spontaneous contacts initiate about an azimuth centered on the impact axis where $r = 0$, as shown in (b) and (c).

wetting front remains symmetrically centered upon the location of initial contact formation as previously described [15]; an example of such a nucleated contact is given in the time series shown in Fig. 3(a). The second mode of contact formation is typified by the near exact correspondence between the location of air film rupture and the globally minimum air film height. Due to the axisymmetry of the air film profile, such events are often clustered closely in time and occur at a nearly identical radial distance from the impact axis. Two examples of this spontaneous mode of contact formation are shown in Figs. 3(b) and 3(c). Sometimes both nucleated and spontaneous contacts are observed in a single droplet impact event. Precisely when a nucleated contact will occur can vary significantly. The air film thickness is not uniform, but instead varies significantly as a function of radius from the impact axis. This can readily be seen in the space-time graphs of the height traces, where the height of closest approach occurs on an annulus near the dimple boundary, but then the liquid lifts away from the surface as it continues to spread over the air film, as reported in prior work [8]. As a consequence, the time to nucleation can in fact be longer than the time for spontaneous contact formation, provided the defect responsible for nucleation is located away from the radial location corresponding to the height of closest approach.

For all contacts, we measure the local height of the air film immediately prior to contact formation, $h_{\min}$, using the last frame recorded. The $h_{\min}$ is plotted as a function of impact velocity in Figs. 4(a) and 4(b). The thin air film is highly sensitive, and over a narrow range of velocities, both rebound and spontaneous wetting are observed for the silicone oil; this range is indicated by the shaded blue region shown in Fig. 4(a) that is bounded on the right-hand side by a thick black line. No rebound events were observed for impact velocities greater than 0.6 m/s. The $h_{\min}$ distribution for nucleated contacts decreases with the impact velocity, as described in detail in Appendix B, and shown in Fig. 7. Notably, the distribution of contact heights is skewed slightly higher for the water-glycerol solution than for the silicone oil droplet impacts.

In the absence of nucleation, spontaneous contact formation is observed only for $h_{\min} < 35$ nm. Below this height, contact is suddenly initiated, forming a capillary bridge that binds the liquid to the solid surface. Notably, for higher-velocity impacts, the resolution of $h_{\min}$ can be limited by the acquisition rate, as the drainage rate of the air film increases with larger U; thus, depending on the

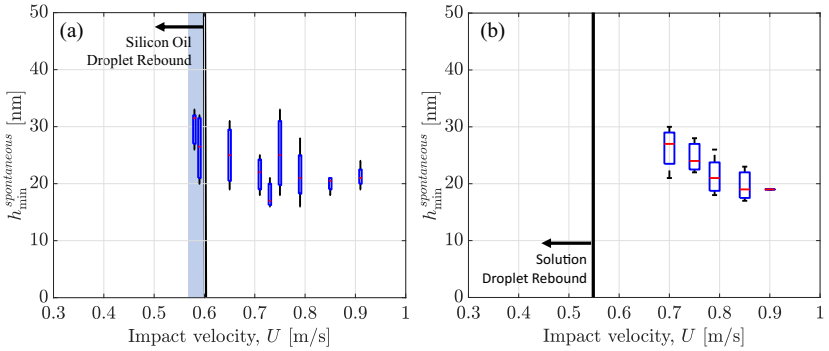

FIG. 4. Box plots of the lowest film height $h_{\min}$ for spontaneous contacts in (a) 36 oil impact events and (b) 18 solution impact events. Open blue boxes indicate the range from the bottom to the top quartile, red lines indicate median values, and black whiskers indicate absolute maximum and minimum values. Spontaneous contact formations are much more frequent for the oil but $h_{\min}$ lies in a range of 18–35 nm for both liquids. Due to the sensitivity of the air film, there is a region over which both rebound events and spontaneous wetting are observed for the oil in (a); this region is indicated by the closed light blue rectangular region near the spontaneous wetting threshold. For $U > 0.6$ m/s, no rebound events are observed. The resolution of the data is limited by the camera's speed and the lower bound of the $h_{\min}$ data is the relevant quantity, i.e., $h_{\min} = 18 \pm 3$ nm for both the liquids. Minimum $h_{\min}$ do not change with the impact speed. This is evident for the silicone oil. The data density for the solution is less dense for spontaneous impacts; still, any changes observed (approximately 7 nm) in $h_{\min}^{\text{spontaneous}}$ are within the tolerance of the profilometry measurement, which at a given pixel is $+7$ or -3 nm. Despite several tries, we did not observe any spontaneous contact formation for moderate velocities of water-glycerol droplet impact, $U < 0.7$ m/s.

phase of the image acquisition and the contact formation, a different value of $h_{\min}$ might be recorded. For each value of U, we repeat experiments several times and thus serendipitously capture lower values of $h_{\min}$, where the image recorded corresponds to the time immediately prior to contact. In this way, the lower bound of $h_{\min}$ data is the relevant quantity. The height $h_{\min} = 18$ ($+7$ or -3) nm for both the silicone oil and the water-glycerol solution. Notably, spontaneous contact occurs much more frequently for the oil than for the water-glycerol solution; this occurs because nucleation is sporadically observed to occur at larger $h_{\min}$ for the water-glycerol solution, as described in detail in Appendix B. For all spontaneous contacts, $h_{\min}$ falls in a range of 18–30 nm for both liquids. The $h_{\min}$ for spontaneous contact does not change considerably with the impact speed. The changes observed are within the tolerance of our measurement accuracy, at $+7$ or -3 nm.

Analysis of the nucleated and spontaneously formed contacts can provide insight into the mechanisms responsible for air film instability and the transition to contact. Following analysis of prior measurements [28] made without the careful calibration as described in Appendix A, we evaluated the statistics of $h_{\min}$ as well as the time from when the air film first forms to contact initiation, t_c. The dynamics of air film rupture is depicted graphically by plotting the film height at $r_{\min}$ as a function of the angle Θ for two impact velocities, $U = 0.58$ and 0.91 m/s, in Figs. 5(b) and 5(c). The angle Θ is defined schematically in Fig. 5(a). For U slightly greater than the critical velocity for droplet rebound, the air film is perforated discretely, with capillary bridges formed from the liquid closest to the surface; however, there can be a significant delay between the first air film rupture event and the final air film rupture event, Δt_C. For much higher velocity impacts, contacts appear to form much more quickly, so the air film appears to rupture symmetrically from the liquid closest to the surface, within the time resolution of our imaging. As U increases, we find that there is an initially steep dropoff in t_c and that t_c continues to fall with U until it reaches the limit set by our image acquisition rate, as shown in Fig. 5(d). The standard deviation of contact formation times σ_{t_c} similarly falls off rapidly as U increases, as shown in Fig. 5(e). The time for

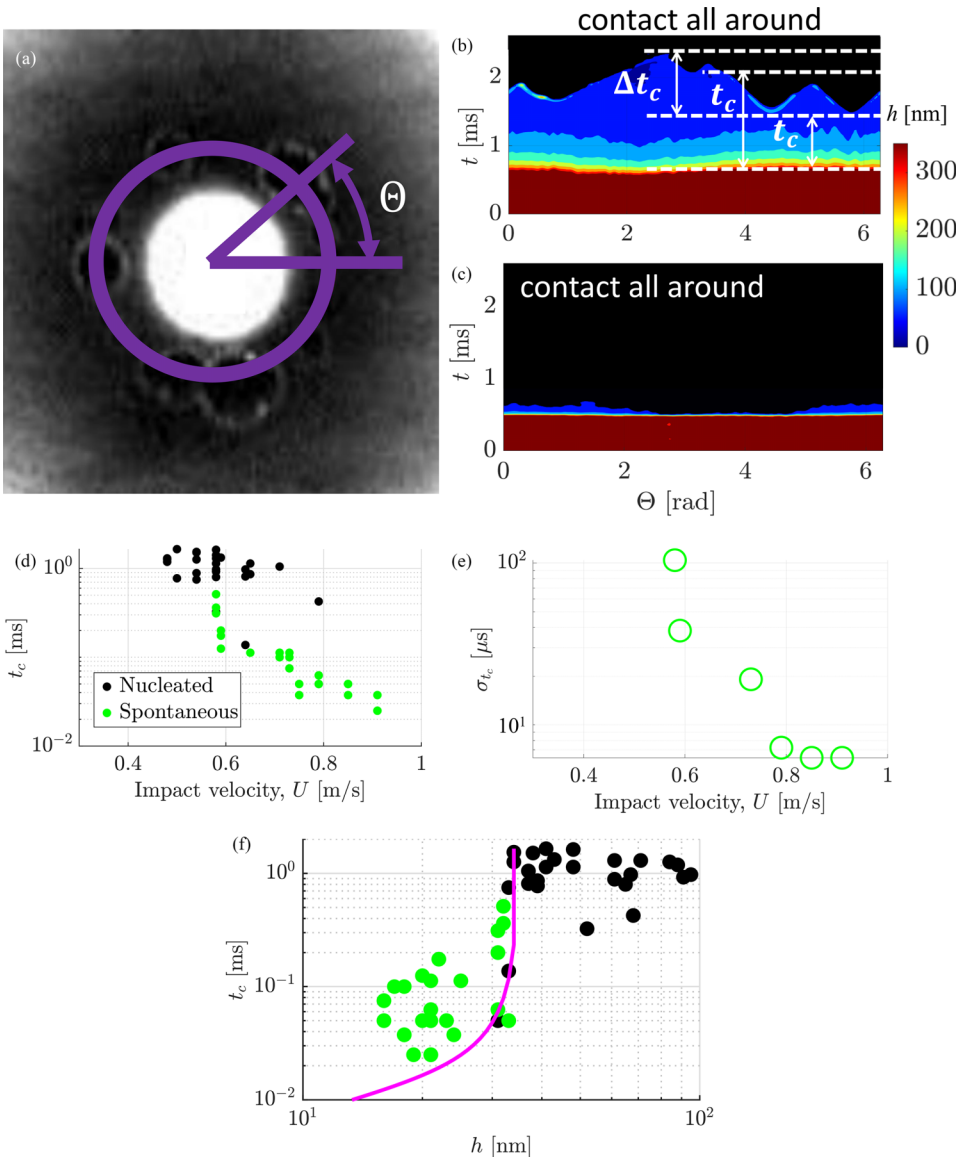

FIG. 5. (a) Initiation of spontaneous contacts occurs on the circumference of a ring at radius $r = r_{\min}$, centered on the impact axis. Kymographs of the evolution of the air film profile and contact along the azimuth defined by Θ, $h(r_{\min}, \Theta, t)$, are shown for silicone oil droplets impacting at velocities of (b) $U = 0.58$ m/s and (c) $U = 0.91$ m/s, respectively. The time between the first passage of the liquid and contact formation, t_c, is indicated for two example spontaneous contact events in (b). The time between a contact's formation and contact all around the azimuth is indicated by Δt_c in (b). At the highest tested impact velocity, where $U = 0.91$ m/s, spontaneous contact occurs nearly simultaneously about the azimuth at $r = r_{\min}$. (d) Plot of t_c for an aggregate total of 53 nucleated (black circles) and spontaneous (green circles) contact events as a function of U; t_c decreases strongly as U increases for the nucleated contact events. (e) Representative time from first spontaneous contact to contact all around the azimuth given by $\sigma_{t_c} = \frac{1}{N-1}\sqrt{\sum_{n=1}^{N-1} \Delta t_{c_n}}$ for N spontaneous contacts; σ_{t_c} decreases suddenly as U increases. The resolution of t_c is set by the inverse of the camera's frame rate. (f) Plot of t_c as a function of the film height immediately prior to contact formation at the location of contact, $h_{\min}$. A comparison of these data with the predictions of linear stability analysis of viscous film dewetting [38] is shown in Appendix C.

contact formation t_c, when compared with the film thickness immediately prior to contact formation h, shows a clear separation between spontaneous events and nucleated events, with minimal overlap near the transitional value of h, as shown in Fig. 5(f).

IV. DISCUSSION

We presented calibrated measurements of the nanometer-scale air film that forms prior to liquid solid contact during droplet impact. With our measurements, we identified two distinct forms of contact initiation, nucleated and spontaneous, that are distinguished by the relative location of the localized wetting bridge and the location where the air film is most thin. For nucleated contacts, there is no correlation between these locations, whereas for spontaneous rupture events, there is nearly exact coincidence between the location of contact formation and the thinnest region of the air film. Experiments were conducted with silicone oil and water-glycerol mixtures, and the surface of impact is carefully cleaved atomically smooth mica. Water-glycerol solution droplets tend to nucleate contact from greater heights than silicone oil droplets; however, both form contact spontaneously from a narrow distribution of film thicknesses, ranging from a minimum of 18 nm to a maximum of approximately 30 nm, with a measurement error of less than 8 nm.

A natural question arises in considering the stability of the air film: What possible mechanisms could cause the air film to rupture and liquid-solid contact to form at a discrete point? Mechanical disruption of the air layer is the most common cause of contact initiation on glass surfaces, but for atomically smooth mica, this is no longer the case. When mechanical nucleation sites are not present, other mechanisms become dominant. A few candidate mechanisms include gas kinetics or finite Knudsen number effects, electrostatic charge, and dipole-dipole interactions typically called van der Waals forces. These have been analyzed or explored in prior works, both theoretically [12] and experimentally [26]; however, controlled experiments with calibrated measurement of the air film thickness have been lacking. With relatively small error bars and repeated experiments, we identified the tightly bound range of heights immediately prior to local destabilization of the air film. Attempts to distinguish the spontaneous from the nucleated contact events on the $t_c(h_{\min})$ graph using the fastest growing mode from linear stability analysis of viscous films [38] did not uniquely separate the two contact populations, making it impossible to distinguish spinodal dewetting from other possible mechanisms of contact formation on atomically smooth mica. Details of this analysis can be found in Appendix C, along with a graph of the timescale for linear instability and the $t_c(h_{\min})$ data.

The transition from droplet rebound to spontaneous contact is immediate for silicone oil; the oil drop either bounces or creates a ring of contact, as shown in Figs. 3(b) and 3(c). By contrast, for the water-glycerol droplets, there is a finite velocity range of $U = 0.55$–0.7 m/s, wherein no rebound or spontaneous contacts were observed, but instead all the contacts were nucleated. Despite the great care taken in our experiments, we did not observe any spontaneous contact formation for this range of impact velocities of solution impact, as can be seen in Fig. 7(b). One possible cause of this discrepancy is electrostatic charge of the solution-air interface, which might be more charged than the silicone oil–air interface, due to the higher dielectric constant of the solution [39] in an electrically noisy environment. Indeed, pure silicone oil droplets do not contain any ions and counterions and thus a Maxwell stress will not develop even in strong electrical fields [40]. As the mica was prepared in the same way for each experiment, we assumed a similar static charge distribution on the mica surface [41]. Thus, it is possible that the solution-air interface contained some static charges that trigger nucleated contact over the intermediate range of impact velocity, where nucleation took place before spontaneous rupture of the air film. This hypothesis is consistent with the large height values of nucleated contacts for the water-glycerol solution droplets, as described in detail in Appendix B.

Our results suggest a universal mechanism for spontaneous contact formation of wetting droplets through intervening air; however, what this mechanism is remains an open question. Electrostatics

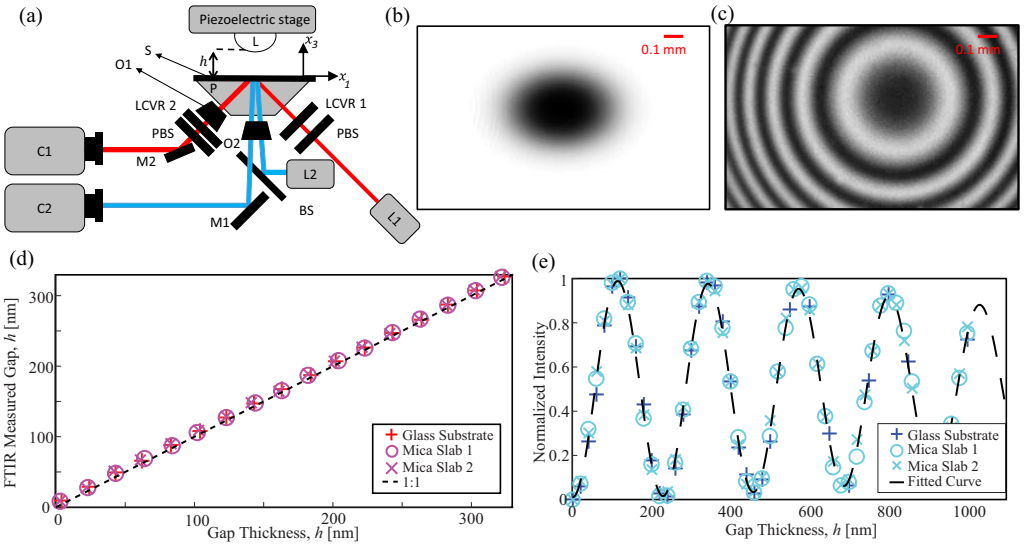

FIG. 6. (a) The setup used for calibration is similar to that of Fig. 1(a) with the nozzle-luer setup replaced by a nanometer-precise piezoelectric stage (Newport three-axis piezoelectric stage with strain gauge feedback control). The spherical lens L made out of smooth N-BK7 glass is glued to the stage face. We lower the stage with steps of $\Delta x_3 = 20$ nm, quasistatically, until the contact occurs and the lens bottom touches the substrate. We calibrate the setup for both mica and glass as solid substrate S; however, we only used mica for the droplet impact studies reported in this paper. (b) The normalized TIR image and (c) the FIF image at the last step are shown. (d) The TIR microscopy is accurate with a maximum error of $+7$ or -3 nm in the range of 0–350 nm irrespective of the substrate used. (e) The universal lookup table for our light source and FIF microscopy setup is applicable to different substrates that we examined as long as the captured images are normalized with respect to the dark and bright field [37]. The horizontal axes of (d) and (e) are the readings from the piezoelectric stage.

might destabilize the air film. Such robustness of the thickness scale for silicone oil suggests that numerical calculations might simply assume contact at this distance, reducing the requisite resolution for accurate numerical modeling of contact phenomena. How this observation is affected by air pressure or applied fields remains to be determined.

APPENDIX A: MICROSCOPY SETUP AND CALIBRATION

The air film thickness measurements are validated by calibration carried out with the simultaneous TIR and FIF microscopy methods. The optical configurations for both methods are depicted in Fig. 6(a). Solid substrates are optically coupled with immersion oil (Nikon) to the top of a dove prism (Thorlabs, BK-7 glass).

In the TIR method [3,8,10,42], the impact surface is illuminated from below with a 5-mW laser with wavelength $\lambda_{\mathrm{TIR}} = 635$ nm (Arima lasers). The laser is mounted in a temperature-controlled mount (model TCLDM9, Thorlabs). The collimated laser light is aligned to be incident at an angle greater than the critical angle for total internal reflection at a substrate-air interface but smaller than the critical angle at the substrate-liquid interface. The reflected light is imaged by a long-working-distance objective (Mitutoyo) and tube lens (Thorlabs) onto the sensor of a high-speed camera (Photron Fastcam Nova S12). After normalization by the background light intensity, the image intensity is directly related to the air layer thickness by a deterministic transfer function [31] provided the light at the substrate-air interface is linearly polarized. Because we often use mica as the substrate and mica is weakly birefringent, we must pre- and postcompensate the polarization

of the light. This is achieved using two polarizing beam splitters (Thorlabs) and two liquid-crystal variable retarders (LCVRs) (Meadowlark), which can programmatically control the polarization state of the light.

Notably, the optical properties of mica sheets may differ from one experiment to the next; thus, we incorporate a photodiode (model S5792, Hamamatsu) aligned at the output of the second polarizing beam splitter. The intensity measurements made with this photodiode are used to determine the unknown parameters in our optical setup. We introduce $\mathfrak{n}_G$, $\mathfrak{n}_S$, ϕ_0, Φ_1 and Φ_2, and $\mathcal{E}$ as refractive indices of air (gas), solid (substrate), the light angle of incident (equal to 45°), the retardance angles of the two LCVRs, and the light electric field, respectively. In TIR with linearly polarized light, for a given weakly birefringent substrate with an arbitrary optical axis (Ψ_S), extended Jones matrix algebra [43] gives the electric field vector $\mathcal{E}$ as the known functions:

$$\mathcal{E}^{\text{out}} = [\mathcal{E}_{\perp}^{\text{out}}, \mathcal{E}_{\parallel}^{\text{out}}]^T = F(\mathfrak{n}_G, \phi_0, \Phi_1, \Phi_2, \mathfrak{n}_S, \Psi_S, \mathcal{E}^{\text{in}}), \tag{A1}$$

$$\mathcal{E}^{\text{SG}} = [\mathcal{E}_{\perp}^{\text{out}}, \mathcal{E}_{\parallel}^{\text{out}}]^T = G(\mathfrak{n}_G, \phi_0, \Phi_1, \mathfrak{n}_S, \Psi_S, \mathcal{E}^{\text{in}}), \tag{A2}$$

where the superscripts in, out, and SG specify the input, the output as measured at the photodiode, and the substrate-air interface, respectively; additionally, the subscripts $\perp$ and $\parallel$ denote the *s*-polarized and *p*-polarized components of the light electric field, respectively. The two polarizing beam splitters in our setup ensure that the *s*-polarized portion of the electric field

$$\mathcal{E}_{\perp}^{\text{in,out}} = 0. \tag{A3}$$

The photodiode measures theoretical $|\mathcal{E}_{\parallel}^{\text{out}}|^2$, quantified by $|\mathcal{E}_{\parallel}^{\text{PD}}|^2$. The values of $\mathfrak{n}_S$ and Θ_S are not known *a priori*, and measuring them using a refractometer and polarimeter for each substrate is not feasible for repeated studies with freshly cleaved surfaces required of our study of droplet impacts.

To overcome the uncertainty of the orientation of the weakly birefringent mica surface in a given iteration of our experiment, we establish the following procedure to determine the LCVR settings that ensure $\mathcal{E}_{\perp}^{\text{SG}} = 0$, using the following *in situ* measurement protocol.

Step 1. We introduce the space $x = [\mathfrak{n}_S, \phi_0, \Psi_S, \mathcal{E}_{\parallel}^{\text{in}}]$ that is fully determined by a system of four equations; however, to increase the accuracy and robustness of this procedure given the uncertainty of the measured data, we solve for x^{opt} in an optimization problem. Instead of solving four equations, we minimize $(\mathcal{E}_{\parallel}^{\text{out}} - \mathcal{E}_{\parallel}^{\text{PD}})^2$ by sweeping a range of voltages on the LCVRs on 25 discrete points, where the retardations of LCVRs 1 and 2 are set independently among $\frac{\Phi_1}{2\pi} = 0.25, 0.3, 0.4, 0.5, 0.6$ and $\frac{\Phi_2}{2\pi} = 0.2, 0.3, 0.4, 0.5, 0.55$.

Step 2. In this range of retardation values realized in the LCVRs, the function F has the highest sensitivity to the values of $\mathfrak{n}_S$ and Θ_S. The root of F is solved for the desired value of x^{opt} using a nonlinear least-squares optimization routine. To check whether the protocol ran successfully, we verify $\phi_0^{\text{opt}} = 45°$, as is set physically in the optical path. At the end of this step, $\mathfrak{n}_S$ and Θ_S are known.

Step 3. We numerically solve Eq. (1) for Φ_1^{target}, which removes all the unwanted spill $\left(\frac{\mathcal{E}_{\perp}^{\text{SG}}}{\mathcal{E}_{\parallel}^{\text{SG}}} \to 0\right)$ at the substrate-air interface. From Eq. (2), the value of Φ_2^{target} that maximizes $\mathcal{E}^{\text{out}}$ is determined; this ensures we maximize the dynamic range captured on the camera's imaging sensor.

Step 4. The values of Φ_1^{target} and Φ_2^{target} are recorded for each substrate and the corresponding voltage amplitudes are applied to LCVRs.

Calibration of the microscopy techniques employed in this work is essential. To calibrate the measurements directly, we used the same optical elements of Fig. 1(a) to track a prescribed trajectory of a rigid glass lens surface in the field of view. To prescribe the trajectory with sufficient accuracy, a piezoelectric stage with nanometer precision and position feedback via strain gauges

(NPC3SG, Newport) was used, as shown in Fig. 6(a). A fixed reference geometry in the form of a spherical glass lens (Thorlabs, $f = 0.25$ m) was affixed to the stage surface and swept stepwise in the $-x_3$ direction starting from $h \approx 350$ nm with a step size of 20 nm until the lowest points of the lens touched the substrate. At each step of the piezoelectric stage, the synchronized cameras record 250 FIF and 250 TIR images at 125 fps. Vibrational noise was reduced by rigid mounts and Sorbothane sheets inserted between the stage and the optical surface. Despite these measures to control unwanted vibration, mechanical noise with an amplitude of approximately 20 nm remained; to filter this noise, we took the median of the recorded images at each step of the piezoelectric stage. The position of the stage at which contact occurs is evident from the lens profile recorded by the cameras [Figs. 6(b) and 6(c)]. Upon contact initiation, mechanical vibrations are no longer measurable. For calibration redundancy, hundreds of control points on the glass lens surface were probed in each image.

The TIR images were resized in the x_2 direction and the intensity was mapped to the gap as described elsewhere [31,34]. The calibration procedure was repeated for different mica sheets and glass substrates; the maximum absolute error in profilometry was found to be less than 7 nm for gaps from $h = 0$ to 350 nm, as shown in Fig. 6(d).

The FIF imaging [37] is conducted along a second optical path with a single-color LED as shown in Fig. 6(a). The FIF optical path is oriented perpendicular to the substrate surface. Unpolarized light from from a high-power blue LED (ILS Solutions) with a peak wavelength of 455 nm is collimated and directed onto the optical path using a 50:50 beam splitter. The light is then focused on the substrate surface by a long-working-distance microscope objective (Mitutoyo 5×). The interference between the two reflected beams from the varying gap results in a pattern of fringes. The fringes are imaged onto the sensor of a second high-speed camera (Photron S12).

The FIF method can extend the depth of field of the gap profilometry to gaps approaching several microns [37]. The mapping function from intensity measurements carried out by the monochromatic FIF modality generates uncertainties in the interpretation of the interferogram due to a finite angle of incidence of the light and the finite light source spectrum [37,44,45]. To address these sources of uncertainty, we recorded images of a known geometry attached to a nanometer-precise piezoelectric driven stage, shown in Fig. 6(e). The FIF images are normalized with respect to the dark and bright fields [37]. We found the mapping function to be universal and fits any point trajectory on the calibration lens even by changing the substrate with an accuracy of $+7$ or -3 nm.

APPENDIX B: NUCLEATION OF CONTACT

Nucleated contacts are distinct from spontaneous contacts due to the random and isolated locations at which they form. This is all the more apparent in the uniformity of the distribution of nucleated contact heights as a function of impact velocity; rather than systematically decreasing, as the globally minimal film thickness h^* does for impact velocities below the bouncing transition impact velocity, nucleated contacts can be observed at heights significantly larger than h^* for a given impact event, even in cases where spontaneous contacts would otherwise form.

To characterize the nature of nucleated contacts, we plot $h_{\min}(U)$ for the silicone oil and the water-glycerol solution in Figs. 7(a) and 7(b), respectively. Whereas the distribution of nucleated contacts for the silicone oil is heavily weighted toward greater proximity to the surface, the same is not true of the contacts formed by impacting droplets of the water-glycerol solution, which are observed at a far greater mean height, with much greater spread, as can be seen in Figs. 7(a) and 7(b), inset. The difference is unlikely to be exclusively dominated by the different nature of mica surfaces, which for all experiments are prepared identically; rather, some other mechanism of contact formation may be at play for contacts between the water-glycerol solution and the mica. Electrostatic charges might be responsible for the observed difference, because of the different dielectric properties of the silicone oil and water-glycerol solution, but tests of droplet charging in the ambient environment were inconclusive.

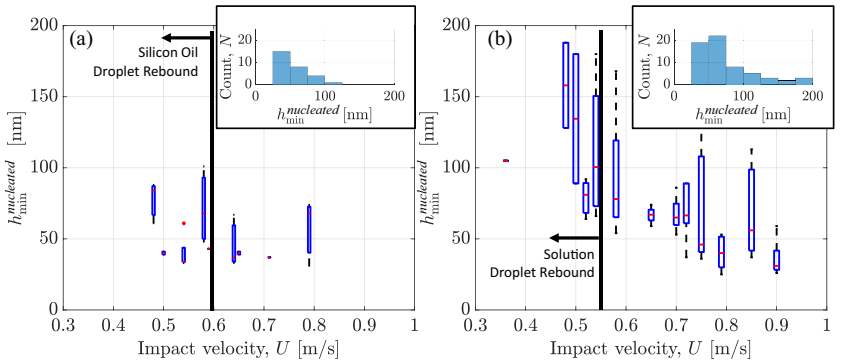

FIG. 7. For nucleated contact formation between the liquid and the solid, the lowest film heights $h_{\min}$ are shown for (a) the silicone oil and (b) the water-glycerol solution. The distribution of $h_{\min}$ appears to be randomly distributed, albeit with much greater nucleation heights for the water-glycerol droplets for impacts below the threshold rebound velocity. Out of 91 impact experiments with silicone oil, 38 droplets bounced, 36 droplets made spontaneous contact, and 17 droplets made contact via nucleation. In the experiments with the solution droplets, from a total of 93, only 15 droplets bounced, 18 droplets made spontaneous contact, and 60 droplets made contact via nucleation.

APPENDIX C: LINEAR STABILITY ANALYSIS OF THE AIR FILM

The linear stability of a viscous film between a liquid and a solid surface subject to destabilizing interfacial forces [46] and surface tension has been evaluated in prior work [22], and film stability has been probed experimentally for polymer films on silicon wafers [23]. During droplet impact, the strong resistance to further drainage in the confined air film generates a configuration similar to that typically found in spinodal dewetting of viscous films [38]. Whereas this analysis assumes a steady film thickness h_0, in our experiments the film thickness evolves slowly; such dynamics may alter the analysis, as the fastest growing mode and the associated growth rate are strong functions of the film thickness [38]. Furthermore, the existing analysis assumes that the thin film is more viscous than the outer fluid phase and that the density of the fluid phases does not alter the dynamics. These assumptions might apply for the droplet impact problem, because the Reynolds numbers in both the droplet and the air film are much less than one [47], and thus the density of the fluid phases should not enter. In this analysis, a timescale for linear instability τ is given in terms of the interfacial force parameter given by the Hamaker constant A and the wave number k of the instability as

$$\frac{1}{\tau} = -\frac{k^2 h^3}{3\eta}\left(\gamma k^2 + \frac{A}{2\pi h^4}\right). \tag{C1}$$

Here $k = 2\pi/\lambda$ is the wave number of the instability, with λ the wavelength; η is the air viscosity; γ is the liquid surface tension; and h is the steady-state film thickness. To determine the fastest growing mode k^*, we maximize $1/\tau$ and obtain, for negative A,

$$k^* = \sqrt{\frac{|A|}{4\pi\gamma h^4}};$$

the associated fastest timescale τ^* is given by

$$\frac{1}{\tau^*} = \left(\frac{|A|^2}{48\eta\gamma\pi^2}\right)h^{-5}.$$

In order to compare our measurements with the theory, we must postulate values for the Hamaker constant. In the absence of a directly measured Hamaker constant for silicone oil and mica across

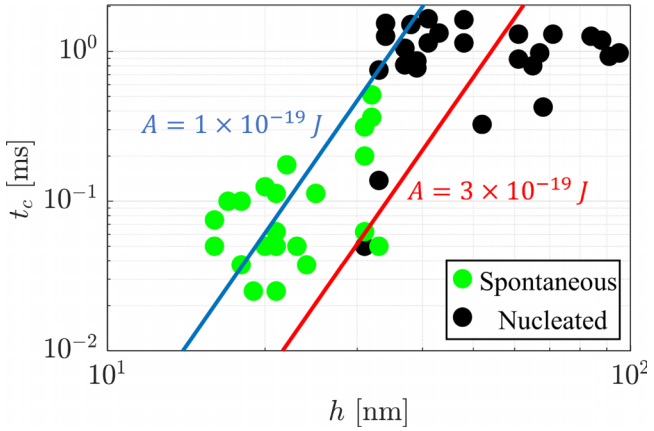

FIG. 8. Results of linear stability analysis. The data shown in Fig. 5(f), consisting of the time from air film formation to contact t_c as a function of the height immediately prior to contact h, are plotted here with the timescale for the fastest growing mode τ^* resulting from the linear stability analysis of a viscous film [38] for two values of the Hamaker constant, $|A| = 1\times10^{-19}$ J in blue and $|A| = 3\times10^{-19}$ J in red. Neither of these predictions clearly defines the boundary between the spontaneous and nucleated contact events, suggesting the possibility that the linear stability analysis does not completely describe the mechanism of contact formation beneath the impacting droplet.

air, we take the measured value of the Hamaker constant for mica interacting with mica across air, calculated with Lifshitz theory to be -1×10^{-19} J and measured to be -1.35×10^{-19} J [46]; for this value of A, the fastest growing timescale is plotted as a function of $h_{\min}$ and shown by the blue line in Fig. 8, along with the $t_c(h_{\min})$ data from Fig. 5(f). As suggested by recent calculations, the value for the Hamaker constant can be modified by gas kinetic effects [12] and may increase in magnitude; to reflect this possibility, the predicted timescale for $|A| = 3\times10^{-19}$ J is shown by the red line in Fig. 8. Irrespective of the value of A used in the analysis, the predicted $\tau(h)$ curve does not demarcate the apparent boundary between the spontaneous and nucleated contact events observed in the experiments, as shown in Fig. 8. Instead, the linear stability prediction generates a line that passes through some of the spontaneous data. This suggests that the linear stability analysis for viscous films may not fully account for the dynamics governing the rupture of the air film.

[1] C. Josserand and S. Thoroddsen, Drop impact on a solid surface, Annu. Rev. Fluid Mech. **48**, 365 (2016).
[2] S. Mandre, M. Mani, and M. P. Brenner, Precursors to splashing of liquid droplets on a solid surface, Phys. Rev. Lett. **102**, 134502 (2009).
[3] J. M. Kolinski, S. M. Rubinstein, S. Mandre, M. P. Brenner, D. A. Weitz, and L. Mahadevan, Skating on a film of air: Drops impacting on a surface, Phys. Rev. Lett. **108**, 074503 (2012).
[4] R. C. A. van der Veen, T. Tran, D. Lohse, and C. Sun, Direct measurements of air layer profiles under impacting droplets using high-speed color interferometry, Phys. Rev. E **85**, 026315 (2012).
[5] W. Bouwhuis, R. C. A. van der Veen, T. Tran, D. L. Keij, K. G. Winkels, I. R. Peters, D. van der Meer, C. Sun, J. H. Snoeijer, and D. Lohse, Maximal air bubble entrainment at liquid-drop impact, Phys. Rev. Lett. **109**, 264501 (2012).
[6] J. de Ruiter, J. M. Oh, D. van den Ende, and F. Mugele, Dynamics of collapse of air films in drop impact, Phys. Rev. Lett. **108**, 074505 (2012).
[7] S. Mandre and M. P. Brenner, The mechanism of a splash on a dry solid surface, J. Fluid Mech. **690**, 148 (2012).

[8] J. M. Kolinski, L. Mahadevan, and S. M. Rubinstein, Lift-off instability during the impact of a drop on a solid surface, Phys. Rev. Lett. **112**, 134501 (2014).
[9] S. Mishra, S. M. Rubinstein, and C. H. Rycroft, Computing the viscous effect in early-time drop impact dynamics, J. Fluid Mech. **945**, A13 (2022).
[10] J. M. Kolinski, L. Mahadevan, and S. Rubinstein, Drops can bounce from perfectly hydrophilic surfaces, Europhys. Lett. **108**, 24001 (2014).
[11] J. de Ruiter, R. Lagraauw, D. van den Ende, and F. Mugele, Wettability-independent bouncing on flat surfaces mediated by thin air films, Nat. Phys. **11**, 48 (2015).
[12] M. V. Chubynsky, K. I. Belousov, D. A. Lockerby, and J. E. Sprittles, Bouncing off the walls: The influence of gas-kinetic and van der Waals effects in drop impact, Phys. Rev. Lett. **124**, 084501 (2020).
[13] S. T. Thoroddsen, K. Takehara, and T. G. Etoh, Bubble entrapment through topological change, Phys. Fluids **22**, 051701 (2010).
[14] H. Y. Lo, Y. Liu, and L. Xu, Mechanism of contact between a droplet and an atomically smooth substrate, Phys. Rev. X **7**, 021036 (2017).
[15] J. M. Kolinski, R. Kaviani, D. Hade, and S. M. Rubinstein, Surfing the capillary wave: Wetting dynamics beneath an impacting drop, Phys. Rev. Fluids **4**, 123605 (2019).
[16] D. Roy, S. S. Rao, and S. Basu, Droplet impact on immiscible liquid pool: Multi-scale dynamics of entrapped air cushion at short timescales, Phys. Fluids **34**, 052004 (2022).
[17] J. C. Burton and P. Taborek, Role of dimensionality and axisymmetry in fluid pinch-off and coalescence, Phys. Rev. Lett. **98**, 224502 (2007).
[18] W. Yuan, T. Wei, and M. Zhang, Dynamical vapour pocket of an impacting leidenfrost droplet: Evaporation and scaling relations, Int. J. Heat Fluid Flow **95**, 108965 (2022).
[19] D. Panchanathan, P. Bourrianne, P. Nicollier, A. Chottratanapituk, K. K. Varanasi, and G. H. McKinley, Levitation of fizzy drops, Sci. Adv. **7**, eabf0888 (2021).
[20] J. de Ruiter, D. van den Ende, and F. Mugele, Air cushioning in droplet impact. II. Experimental characterization of the air film evolution, Phys. Fluids **27**, 012105 (2015).
[21] Y. Gao, S. Jung, and L. Pan, Interaction forces between water droplets and solid surfaces across air films, ACS Omega **4**, 16674 (2019).
[22] F. B. Wyart and J. Daillant, Drying of solids wetted by thin liquid films, Can. J. Phys. **68**, 1084 (1990).
[23] G. Reiter, A. Sharma, A. Casoli, M.-O. David, R. Khanna, and P. Auroy, Thin film instability induced by long-range forces, Langmuir **15**, 2551 (1999).
[24] M. Pack, H. Hu, D. Kim, Z. Zheng, H. A. Stone, and Y. Sun, Failure mechanisms of air entrainment in drop impact on lubricated surfaces, Soft Matter **13**, 2402 (2017).
[25] K. Langley, E. Q. Li, and S. T. Thoroddsen, Impact of ultra-viscous drops: Air-film gliding and extreme wetting, J. Fluid Mech. **813**, 647 (2017).
[26] F. Gao, H. Yi, L. Qi, R. Qiao, and W. Deng, Weakly charged droplets fundamentally change impact dynamics on flat surfaces, Soft Matter **15**, 5548 (2019).
[27] A. Latka, A. Strandburg-Peshkin, M. M. Driscoll, C. S. Stevens, and S. R. Nagel, Creation of prompt and thin-sheet splashing by varying surface roughness or increasing air pressure, Phys. Rev. Lett. **109**, 054501 (2012).
[28] J. M. Kolinski, The role of air in droplet impact on a smooth, solid surface, Ph.D. thesis, Harvard University, 2015.
[29] S. J. Weinstein and K. J. Ruschak, Coating flows, Annu. Rev. Fluid Mech. **36**, 29 (2004).
[30] L. Xu, W. W. Zhang, and S. R. Nagel, Drop splashing on a dry smooth surface, Phys. Rev. Lett. **94**, 184505 (2005).
[31] M. Shirota, M. A. J. van Limbeek, D. Lohse, and C. Sun, Measuring thin films using quantitative frustrated total internal reflection (FTIR), Eur. Phys. J. E **40**, 54 (2017).
[32] M. M. Driscoll and S. R. Nagel, Ultrafast interference imaging of air in splashing dynamics, Phys. Rev. Lett. **107**, 154502 (2011).
[33] M. Pack, P. Kaneelil, H. Kim, and Y. Sun, Contact line instability caused by air rim formation under nonsplashing droplets, Langmuir **34**, 4962 (2018).

[34] P. Chantelot and D. Lohse, Drop impact on superheated surfaces: Short-time dynamics and transition to contact, J. Fluid Mech. **928**, A36 (2021).
[35] R. Kaviani and J. M. Kolinski, High resolution interferometric imaging of liquid-solid interfaces with HOTNNET, Exp. Mech. **63**, 309 (2023).
[36] L. Zhang, T. Soori, A. Rokoni, A. Kaminski, and Y. Sun, Thin film instability driven dimple mode of air film failure during drop impact on smooth surfaces, Phys. Rev. Fluids **6**, 044002 (2021).
[37] J. O. Rädler and E. Sackmann, Imaging optical thicknesses and separation distances of phospholipid vesicles at solid surfaces, J. Phys. (France) II **3**, 727 (1992).
[38] P.-G. Gennes, F. Brochard-Wyart, and D. Quéré, *Capillarity and Wetting Phenomena: Drops, Bubbles, Pearls, Waves* (Springer, New York, 2004).
[39] R. Behrends, K. Fuchs, U. Kaatze, Y. Hayashi, and Y. Feldman, Dielectric properties of glycerol/water mixtures at temperatures between 10 and 50 °C, J. Chem. Phys. **124**, 144512 (2006).
[40] R. Granda, G. Li, V. Yurkiv, F. Mashayek, and A. L. Yarin, Dielectrophoretic stretching of drops of silicone oil: Experiments and multi-physical modeling, Phys. Fluids **34**, 042108 (2022).
[41] H. K. Christenson and N. H. Thomson, The nature of the air-cleaved mica surface, Surf. Sci. Rep. **71**, 367 (2016).
[42] S. M. Rubinstein, G. Cohen, and J. Fineberg, Detachment fronts and the onset of dynamic friction, Nature (London) **430**, 1005 (2004).
[43] C. Gu and P. Yeh, Extended Jones matrix method II, J. Opt. Soc. Am. A **10**, 966 (1993).
[44] J. Schilling, K. Sengupta, S. Goennenwein, A. Bausch, and E. Sackmann, Absolute interfacial distance measurements by dual-wavelength reflection interference contrast microscopy, Phys. Rev. E **69**, 021901 (2004).
[45] J. de Ruiter, F. Mugele, and D. van den Ende, Air cushioning in droplet impact. I. Dynamics of thin films studied by dual wavelength reflection interference microscopy, Phys. Fluids **27**, 012104 (2015).
[46] J. Israelachvili, *Intermolecular and Surface Forces*, 3rd ed. (Academic Press, New York, 2011).
[47] To estimate the Reynolds number in the gas phase, we use the slow variation of the air film thickness during rebound, as plotted in Fig. 2(f). The inertial pressure of the droplet $p = \rho U^2/2 \approx 500$ Pa confirms that the air compression is negligible for $U \approx 1$ m/s. The lateral velocity of the gas can be estimated by considering the changes in h and applying incompressibility locally. By inspection, h decreases by about 25 nm in 2 ms. Thus, a crude estimate of dh/dt is 12.5 μm/s; this change in height must be balanced by a flux of gas laterally along the air film. From incompressibility, $\nabla \cdot \mathbf{u} = \mathbf{0}$; thus, for an axisymmetric flow where $u_\theta = 0$, $\frac{1}{r}\frac{\partial r u_r}{\partial r} + \frac{\partial u_z}{\partial z} = 0$. Here we assume that the radial direction is given by x and the direction normal to the surface by y and that there is no flow in the azimuthal direction by symmetry. A representative scale of x is 100 μm or more; a representative scale for y is 100 nm or less. Applying these scales, the lateral velocity of the gas is estimated as $u_x = \frac{dx}{dy}u_y = \frac{10^{-4}}{10^{-7}}\dot{h} = 10^3 \times 12.5\,\mu\text{m/s} = 12.5\,\text{mm/s}$. To complete the estimation of Re, we use the air film thickness 100 nm as the length scale, the air density of 1 kg/m^3, and the air viscosity of approximately 2×10^{-5} Pas, resulting in $\text{Re} \approx 6.25\times10^{-5}$; thus, viscous stresses dominate in the air film. Estimating the Reynolds number in the liquid phase is more straightforward. The liquid droplet moves toward the surface at the same velocity as the air film in the vertical direction, estimated at 12.5 μm/s, over a similar lateral scale of 100 μm. The liquid's kinematic viscosity is 20 cSt or 2×10^{-5} m^2/s, resulting in a similar $\text{Re} \approx 6.25\times10^{-5}$. Thus, viscous stresses dominate in both the liquid and the gas during the rebound process.